



## Detecting Ozone- and Greenhouse Gas–Driven Wind Trends with Observational Data

Suyoung Lee and Steven B. Feldstein

*Science* **339**, 563 (2013);

DOI: 10.1126/science.1225154

*This copy is for your personal, non-commercial use only.*

If you wish to distribute this article to others, you can order high-quality copies for your colleagues, clients, or customers by [clicking here](#).

Permission to republish or repurpose articles or portions of articles can be obtained by following the guidelines [here](#).

**The following resources related to this article are available online at [www.sciencemag.org](http://www.sciencemag.org) (this information is current as of April 26, 2013):**

**Updated information and services**, including high-resolution figures, can be found in the online version of this article at:

<http://www.sciencemag.org/content/339/6119/563.full.html>

**Supporting Online Material** can be found at:

<http://www.sciencemag.org/content/suppl/2013/01/30/339.6119.563.DC1.html>

A list of selected additional articles on the Science Web sites **related to this article** can be found at:

<http://www.sciencemag.org/content/339/6119/563.full.html#related>

This article **cites 30 articles**, 3 of which can be accessed free:

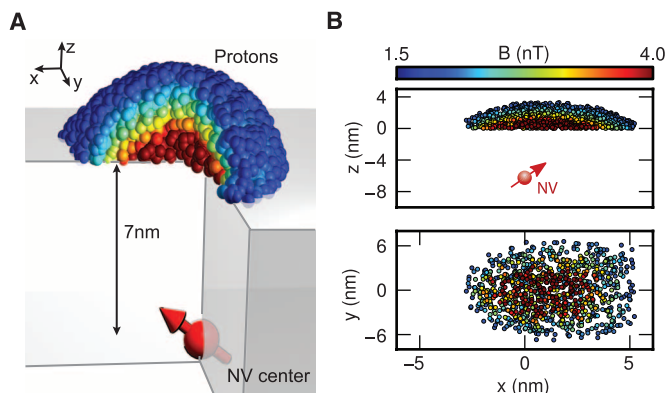
<http://www.sciencemag.org/content/339/6119/563.full.html#ref-list-1>

This article appears in the following **subject collections**:

Atmospheric Science

<http://www.sciencemag.org/cgi/collection/atmos>

**Fig. 4.** Numerical simulation of the detection volume. **(A)** Three-dimensional visualization of the  $10^4$  closest protons (spheres), generating 70% of the signal. Protons are color-coded by their contribution to the total signal. **(B)** Two-dimensional projections of (A).



time scale and broaden the line. Second, the line was substantially broadened by our spectral resolution ( $12.2 \pm 0.3$  kHz, upper curve of Fig. 3B). This experimental resolution could be improved by increasing  $N$ , the order of dynamical decoupling, which should allow for an ultimate resolution of  $\Delta\nu/\nu \approx (T_{1,NV}\Omega_{R,NV})^{-1} \approx 1$  ppm, with  $T_{1,NV}\Omega_{R,NV}$  denoting the relaxation time and Rabi frequency of the NV, respectively (28, 29).

The integrated, background-corrected field strength experienced under a coating of PMMA by a typical NV center is  $B_{\text{rms}} = 390 \pm 60$  nT (green shaded area in Fig. 3A). According to an analytical model of the proton magnetic field (30), assuming a homogeneous proton density of  $5 \times 10^{28} \text{ m}^{-3}$ , this field strength corresponds to an NV center located  $6.4 \pm 0.7$  nm below the surface. Numerical simulations of the ion implantation predict a similar value (17). This suggests that our result can yield a nondestructive method to measure the depth of an individual center with nanometer statistical uncertainty.

We confirmed the signal magnitude by a numerical simulation, which explicitly computes the field of  $4 \times 10^5$  protons, placed at random locations in a cube of 20-nm width. We found that 70% of the signal was generated by the  $10^4$  closest protons, corresponding to a detection volume of only  $(5 \text{ nm})^3$  (Fig. 4), which is comparable to that of a medium-size (100-kD) protein.

An important extension of our results will be the combination with scanning NV centers (14, 15) to implement NMR imaging at the nanoscale. Being based on statistical rather than thermal polarization, our approach enables the acquisition of NMR spectra of an arbitrary substance at low magnetic fields, down to and including zero field, without the need for prepolarization (31). In this regime, magic angle spinning can be realized by rotating the external field rather than the sample. This allows for higher rotation frequencies than at high field, which is potentially of great benefit for solid-state NMR. Finally, we anticipate that our technique can yield a new method of hyperpolarization for arbitrary samples by coherently transferring the polarization of the NV spin to the sample. We estimate that full polarization of the detection volume might be achievable. The transfer of one quan-

tum of angular momentum would occur on the time scale of our detection ( $\sim 20 \mu\text{s}$ ), and hence  $10^4$  transfers can be completed on a time scale faster than the protons' longitudinal relaxation time  $T_1$  (typically on the order of seconds).

#### References and Notes

1. F. Bloch, *Phys. Rev.* **70**, 460 (1946).
2. E. M. Purcell, H. C. Torrey, R. V. Pound, *Phys. Rev.* **69**, 37 (1946).
3. D. Rugar, R. Budakian, H. J. Mamin, B. W. Chui, *Nature* **430**, 329 (2004).
4. C. L. Degen, M. Poggio, H. J. Mamin, C. T. Rettner, D. Rugar, *Proc. Natl. Acad. Sci. U.S.A.* **106**, 1313 (2009).
5. L. Ciobanu, D. A. Seeber, C. H. Pennington, *J. Magn. Reson.* **158**, 178 (2002).
6. A. Blank, J. H. Freed, *Isr. J. Chem.* **46**, 423 (2007).
7. A. Gruber *et al.*, *Science* **276**, 2012 (1997).
8. F. Jelezko, T. Gaebel, I. Popa, A. Gruber, J. Wrachtrup, *Phys. Rev. Lett.* **92**, 076401 (2004).
9. J. M. Taylor *et al.*, *Nat. Phys.* **4**, 810 (2008).
10. G. Balasubramanian *et al.*, *Nat. Mater.* **8**, 383 (2009).
11. T. H. Taminiau *et al.*, *Phys. Rev. Lett.* **109**, 137602 (2012).
12. S. Kolkowitz, Q. P. Unterreithmeier, S. D. Bennett, M. D. Lukin, *Phys. Rev. Lett.* **109**, 137601 (2012).
13. N. Zhao *et al.*, *Nat. Nanotechnol.* **7**, 657 (2012).
14. G. Balasubramanian *et al.*, *Nature* **455**, 648 (2008).
15. P. Maletinsky *et al.*, *Nat. Nanotechnol.* **7**, 320 (2012).
16. J. Meijer *et al.*, *Appl. Phys. Lett.* **87**, 261909 (2005).

17. Supplementary materials are available on Science Online.
18. C. L. Degen, M. Poggio, H. J. Mamin, D. Rugar, *Phys. Rev. Lett.* **99**, 250601 (2007).
19. F. Reinhard *et al.*, *Phys. Rev. Lett.* **108**, 200402 (2012).
20. L. Cywiński, R. M. Lutchny, C. P. Nave, S. Das Sarma, *Phys. Rev. B* **77**, 174509 (2008).
21. G. de Lange, D. Ristè, V. V. Dobrovitski, R. Hanson, *Phys. Rev. Lett.* **106**, 080802 (2011).
22. A. Larauoi, J. S. Hodges, C. A. Meriles, *Appl. Phys. Lett.* **97**, 143104 (2010).
23. S. Kotler, N. Akerman, Y. Glickman, A. Keselman, R. Ozari, *Nature* **473**, 61 (2011).
24. J. Bylander *et al.*, *Nat. Phys.* **7**, 565 (2011).
25. L. T. Hall, J. H. Cole, C. D. Hill, L. C. L. Hollenberg, *Phys. Rev. Lett.* **103**, 220802 (2009).
26. N. Bar-Gill *et al.*, *Nat. Commun.* **3**, 858 (2012).
27. K. M. Sinnott, *J. Polym. Sci., Polym. Phys. Ed.* **42**, 3 (1960).
28. E. C. Reynhardt, G. L. High, J. A. van Wyk, *J. Chem. Phys.* **109**, 8471 (1998).
29. G. D. Fuchs, V. V. Dobrovitski, D. M. Toyli, F. J. Heremans, D. D. Awschalom, *Science* **326**, 1520 (2009).
30. C. A. Meriles *et al.*, *J. Chem. Phys.* **133**, 124105 (2010).
31. M. P. Ledbetter *et al.*, *Proc. Natl. Acad. Sci. U.S.A.* **105**, 2286 (2008).

**Acknowledgments:** We thank L. Häussler, D. Antonov, A. Denisenko, and A. Aird for sharing cTRIM and molecular dynamics simulation data and G. Majer and T. Bräuninger for bulk NMR measurements, as well as H. J. Mamin, D. Rugar, and P.-G. Reinhard for helpful discussions. This work was supported by the European Union (SQUTEC, DIAMANT), the Max Planck Society, Deutsche Forschungsgemeinschaft (SFB/TR21, Research groups 1493 and 1482, SPP1601), Defense Advanced Research Projects Agency (QUASAR program), Volkswagen Foundation, contract research of the Baden-Württemberg foundation ("Methoden für die Lebenswissenschaften"), the 973 Program (2013CB921800), NNSFC (11227901, 91021005, 10834005), and Chinese Academy of Sciences. T.S. acknowledges financial support from the IMPRS-AM and C.A.M. from the Humboldt Foundation and the NSF (NSF-1111410).

#### Supplementary Materials

[www.sciencemag.org/cgi/content/full/339/6119/561/DC1](http://www.sciencemag.org/cgi/content/full/339/6119/561/DC1)  
Materials and Methods  
Supplementary Text  
Figs. S1 to S7  
References (32, 33)

17 October 2012; accepted 3 December 2012  
10.1126/science.1231675

## Detecting Ozone- and Greenhouse Gas-Driven Wind Trends with Observational Data

Sukyong Lee<sup>1\*</sup> and Steven B. Feldstein<sup>1</sup>

Modeling studies suggest that Antarctic ozone depletion and, to a lesser degree, greenhouse gas (GHG) increase have caused the observed poleward shift in the westerly jet during the austral summer. Similar studies have not been performed previously with observational data because of difficulties in separating the two contributions. By applying a cluster analysis to daily ERA-Interim data, we found two 7- to 11-day wind clusters, one resembling the models' responses to GHG forcing and the other resembling ozone depletion. The trends in the clusters' frequency of occurrence indicate that the ozone contributed about 50% more than GHG toward the jet shift, supporting the modeling results. Moreover, tropical convection apparently plays an important role for the GHG-driven trend.

Throughout the late 20th century, the Southern Hemisphere (SH) westerlies have undergone a poleward shift (1–3), especially

during the austral summer (December through February; DJF hereafter) (Fig. 1A). This change affects weather and climate not only by altering the

location of storms but also by influencing the rate of carbon uptake in the Southern Ocean (4, 5) and by decreasing Antarctic snow melt (6). This poleward jet shift is commonly described as a trend toward the positive phase of the Southern Annular Mode (SAM), a pattern that is often defined as the first empirical orthogonal function of the zonal-mean zonal wind (7). Modeling studies found that a positive SAM trend can be simulated either by increasing the atmospheric greenhouse gas (GHG) concentration (8) or by decreasing stratospheric ozone, with the ozone having a greater impact (9, 10). It is unclear to what extent the model-based attributions are valid in nature; similar attribution studies have not been performed with observational data because of the perception that the circulation responses cannot be separated. However, the continuum perspective (11, 12) suggests that the responses to the two forcings may be sufficiently different from each other that a cluster analysis would find them to be distinctive. Although this approach has its own uncertainties, if the response to the forcings inferred from observational data resemble those from model experiments, we can be reasonably confident that the impacts of the individual forcings are being accurately evaluated.

This possibility was explored by applying the method of self-organizing maps (SOMs) (12, 13) to daily DJF zonal-mean zonal wind data from the European Center for Medium-Range Weather Forecasts ERA-Interim reanalysis data set (14). The method partitions the data into a specified number of patterns, referred to as SOM patterns, organized on an ( $m \times n$ ) SOM grid. The SOM patterns are determined by minimizing the euclidean distance (12) between the SOM patterns and the observed fields, yielding patterns that closely resemble the observations. The number of SOM patterns chosen has its basis in two criteria: the number must be large enough to accurately capture the observed daily fields but small enough to conveniently describe the zonal wind anomalies. We quantified this accuracy by calculating pattern correlations between the observed daily fields and the particular SOM pattern for each day that has the smallest euclidean distance from the observed field. From this calculation (summarized in Table 1), we conclude that a ( $4 \times 1$ ) grid meets these two criteria.

The four SOM patterns (Fig. 2, left column) express various degrees of zonal wind variability: The first pattern (first row, referred to as SOM1) corresponds to an equatorward shift of the mid-latitude westerlies; the second pattern (second row, SOM2) also describes an equatorward shift but includes a strong tropical signal; the third pattern (third row, SOM3) coincides with a poleward shift of the westerlies with a weakening in the maximum strength of the jet; and the fourth pattern (fourth row, SOM4) corresponds to a smaller poleward jet shift with a strong tropical component.

Three of the four SOM patterns (except SOM2) coincide with a large-amplitude composite (15) SAM signal (fig. S1). The frequency of occurrence (for brevity, “frequency”) of each SOM pattern was measured by counting the number of days on which the euclidean distance between a particular SOM pattern and the observed pattern is smallest. This yielded a time series of the frequency (Fig. 2, right column). For SOM3, there is a statistically significant ( $P < 0.05$ ) positive linear trend (see the red dashed line). The SOM1 frequency also shows a noticeable trend (the black dashed line), although it is not statistically significant.

The extent to which the trend of individual SOM patterns contributes to the actual observed linear trend can be quantified by multiplying each SOM pattern by the corresponding frequency trend normalized by 90 (DJF) days (16). The result (Fig. 2, middle column) shows that the poleward shift in the westerlies is dominated by contributions from both SOM1 and SOM3, with the latter being roughly 50% greater. The sum of all four SOM-derived trends (Fig. 1B) compares well with the actual trend (Fig. 1A) in most

regions. Because the composite (15) time scales of SOM1 and SOM3 are 11 and 7 days (measured as the average of the time scales over which the composite SOM1 and SOM3 amplitudes grow and decay by a factor of  $e$ ), respectively (fig. S2), our finding indicates that most of the observed poleward jet shift can be explained by the decadal trends in the frequencies of SOM1 and SOM3.

The spatial structures suggest that SOM1 may be linked to GHG warming and SOM3 to stratospheric ozone depletion. Figure 2 shows that SOM1 has a node at the jet center, with one dominant extremum on the equatorward side of the jet that has virtually no vertical tilt. In contrast, SOM3 has a node located slightly poleward of the jet center and three extrema on the equatorward side of the jet, with the two nodes on the equatorward side tilting poleward with height. These characteristics of SOM1 and SOM3 are present in the model responses to GHG forcing [e.g., figure 5b in (8), figure 4b in (10), and figure 3a in (17)] and ozone forcing [figure 3a in (18), figure 4a in (10), and figure 4B in (19)], respectively [figure 4b in (10) is reproduced as fig. S3].

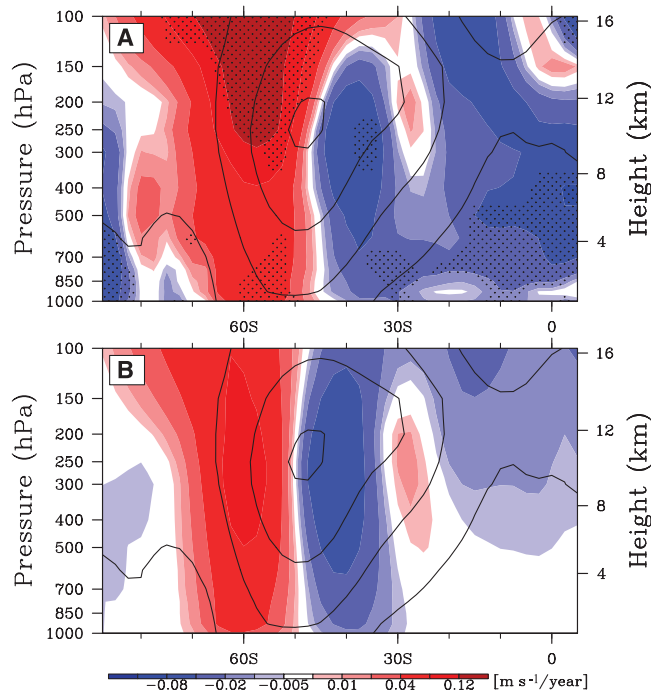


**Fig. 1.** The 1979 to 2008 DJF zonal-mean zonal wind trend: (A) total trend and (B) the sum of the four SOM trends shown in Fig. 2. The solid contours show the climatological zonal-mean zonal wind.

**Table 1.** Pattern correlations between the daily zonal-mean zonal wind and the corresponding SOM pattern for each day, weighted by the corresponding SOM frequency (second column). The third column shows correlations (corr) for SOM1 for the ( $4 \times 1$ ) grid, and SOM1-like patterns for all other grids. When there are more than one SOM1-like patterns, multiple correlations are shown. Similarly, the fourth column shows correlations for SOM3 and SOM3-like patterns.

SOM grid	Mean corr for all SOMs	Corr for SOM1-like pattern	Corr for SOM3-like pattern
(4 × 1)	0.48	0.59	0.66
(5 × 1)	0.51	0.61	0.67
(6 × 1)	0.52	0.69	0.70
(7 × 1)	0.54	0.68	0.73
(8 × 1)	0.55	0.68	0.63/0.75
(9 × 1)	0.58	0.73/0.63	0.75

<sup>1</sup>Department of Meteorology, The Pennsylvania State University, University Park, PA 16802, USA.

\*To whom correspondence should be addressed. E-mail: sxl31@meteo.psu.edu

Figure 3A shows the time series of both DJF global mean temperature [from the National Oceanic and Atmospheric Administration (NOAA) Climatic Data Center], defined here as the deviation from the 1901 to 2000 average, and the SOM1 frequency. (The former time series is used as an indicator of the response to GHG forcing.) At time scales longer than 7 years (low pass), the upper limit of the El Niño–Southern Oscillation (ENSO) time scale, these time series are correlated at  $-0.52$ , whereas for shorter time scales (raw minus low pass; simply “high pass”

hereafter), their correlation is  $0.50$ . Both correlations are significant ( $P < 0.05$ ). The high-pass SOM1 frequency and global mean temperature are correlated with the Niño 3.4 index (Fig. 3B) at values of  $0.75$  and  $0.64$ , respectively, indicating that the positive correlation between the high-pass SOM1 frequency and global mean temperature is likely due to the driving of both quantities by ENSO. Indeed, as indicated by the blue lines in Fig. 2, ENSO influences the SOM1 frequency, whereas its impact is negligible for the remaining SOMs.

How do we then interpret the negative correlation at the low frequencies? We suggest that the answer lies in the fact that GHG driving not only increases the global mean temperature, it also causes a La Niña-like trend in tropical sea surface temperature (20, 21) and convection (22), with both variables exhibiting an increase over Indonesia and a decrease over the central tropical Pacific. This is supported by SOM1 exhibiting both a downward decadal trend in its frequency of occurrence (Fig. 2) and on intra-seasonal time scales by its being associated with

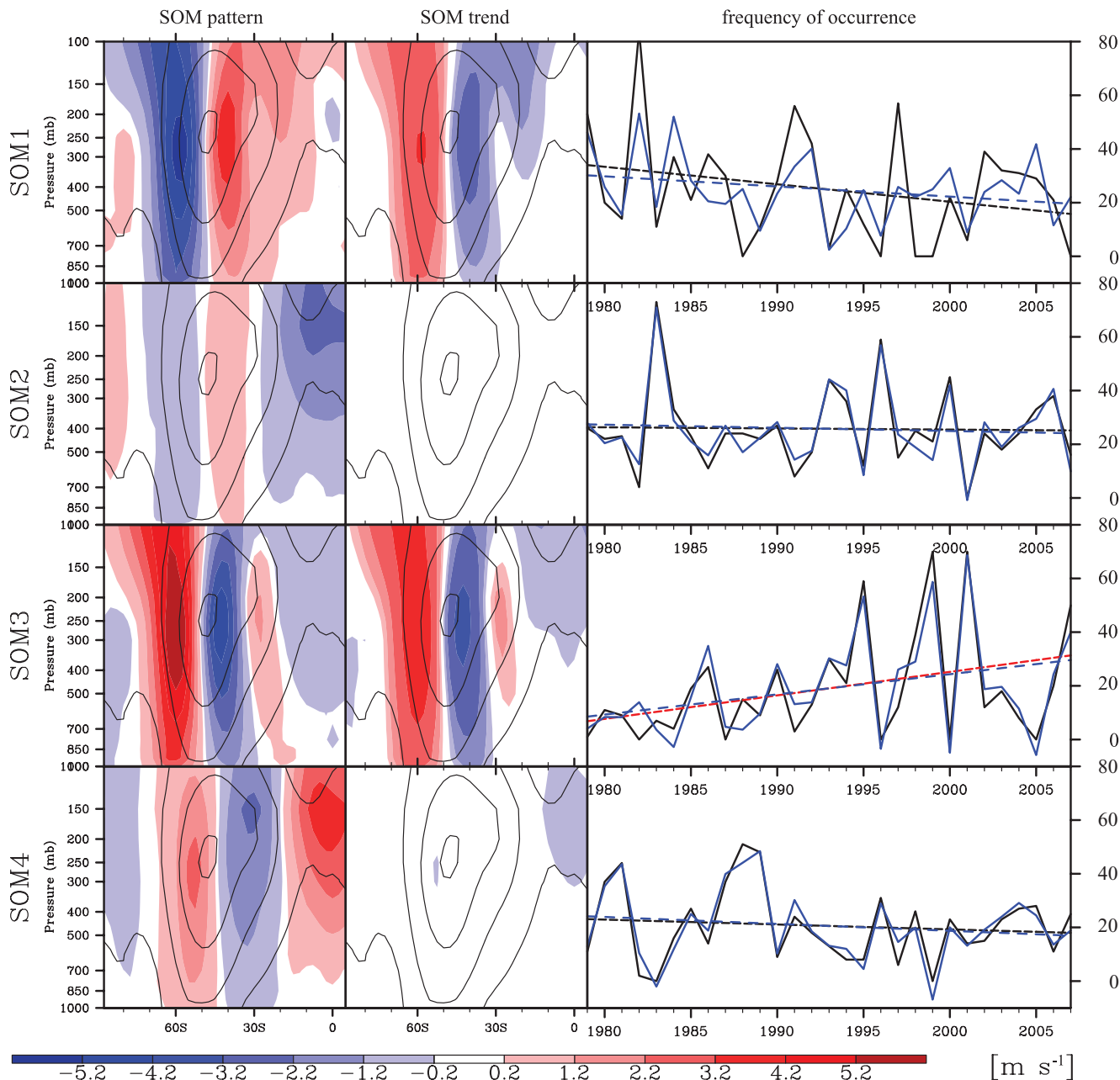


**Fig. 2.** The SOM patterns of the DJF zonal-mean zonal wind for a  $(4 \times 1)$  grid. The left column shows the SOM patterns, the middle column is the 1979 to 2008 trend for each SOM, and the right column shows the frequency time series (solid black line) shown as the number of days for each DJF season. The solid contours in the first two columns show the climatological zonal-mean zonal wind. In the third column, the solid blue lines

are ENSO-removed frequency time series. The dashed black (blue) lines are the least square linear fit of the frequency (ENSO-removed frequency) time series. If the linear fit is statistically significant ( $P < 0.05$ ) based on a Student’s  $t$  test, the dashed black line is replaced by a dashed red line. The color bar is for the first column. The scale for the second column is shown in the color bar of Fig. 1.

Downloaded from www.sciencemag.org on April 26, 2013

an El Niño-like outgoing long-wave radiation (OLR; a proxy of tropical convection intensity) anomaly pattern (fig. S4a) that is opposite in sign to that for La Niña. [If the OLR composite is confined to ENSO neutral years, the La Niña-like convection anomalies remain intact, except in the eastern Pacific (fig. S4b).] The trend in tropical OLR associated with the SOM patterns is dominated by SOM1, and consistently the 1979 to 2008 OLR trend exhibits a La Niña-like OLR structure (fig. S5). This connection between the La Niña-like convection and the poleward jet shift is consistent with previous studies (23, 24).

The SOM3 frequency is not correlated with the global mean temperature and is instead sig-

nificantly correlated at  $-0.45$  ( $P < 0.05$ ) with a November Antarctic ozone index, which we define as the integrated total column ozone anomaly (from ERA-Interim data) poleward of  $75^\circ\text{S}$  (with area weighting), where the reference state for the anomaly is the 1979 to 2008 DJF mean total column ozone. (The SOM1 frequency is uncorrelated with the ozone index.) To facilitate comparison with the SOM3 frequency, we plotted the ozone index with its sign reversed (Fig. 3C). Moreover, the SOM3 frequency time series closely resembles the yearly time series of the calendar date of the stratospheric final warming (25), whose trend toward later dates is attributed to ozone depletion. The final warming occurs most-

ly during December. Consistently, we found that for this month SOM3 occurs most frequently and its trend is positive. A separate SOM analysis for each of the three months, which yields similar patterns, also found that the frequency time series for SOM3-like patterns exhibits the highest correlations with the Antarctic ozone index during December. In contrast, the correlations between SOM1-like frequency series and the global mean temperature were found to be largest during January and February, indicating that the influence of GHG is strongest during the late summer.

The composite temperature structure provides further support for these relationships between the SOM patterns and the external forcings (Fig. 4).

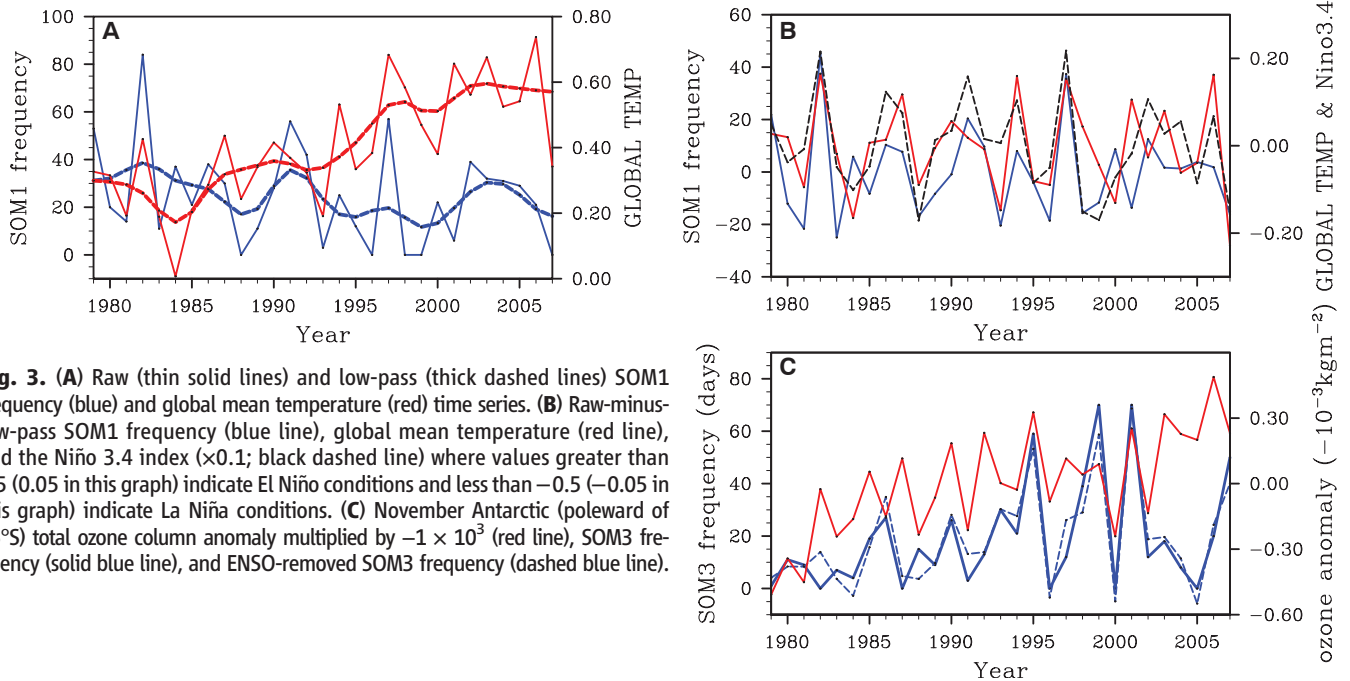


**Fig. 3.** (A) Raw (thin solid lines) and low-pass (thick dashed lines) SOM1 frequency (blue) and global mean temperature (red) time series. (B) Raw-minus-low-pass SOM1 frequency (blue line), global mean temperature (red line), and the Niño 3.4 index ( $\times 0.1$ ; black dashed line) where values greater than 0.5 (0.05 in this graph) indicate El Niño conditions and less than  $-0.5$  ( $-0.05$  in this graph) indicate La Niña conditions. (C) November Antarctic (poleward of  $75^\circ\text{S}$ ) total ozone column anomaly multiplied by  $-1 \times 10^3$  (red line), SOM3 frequency (solid blue line), and ENSO-removed SOM3 frequency (dashed blue line).

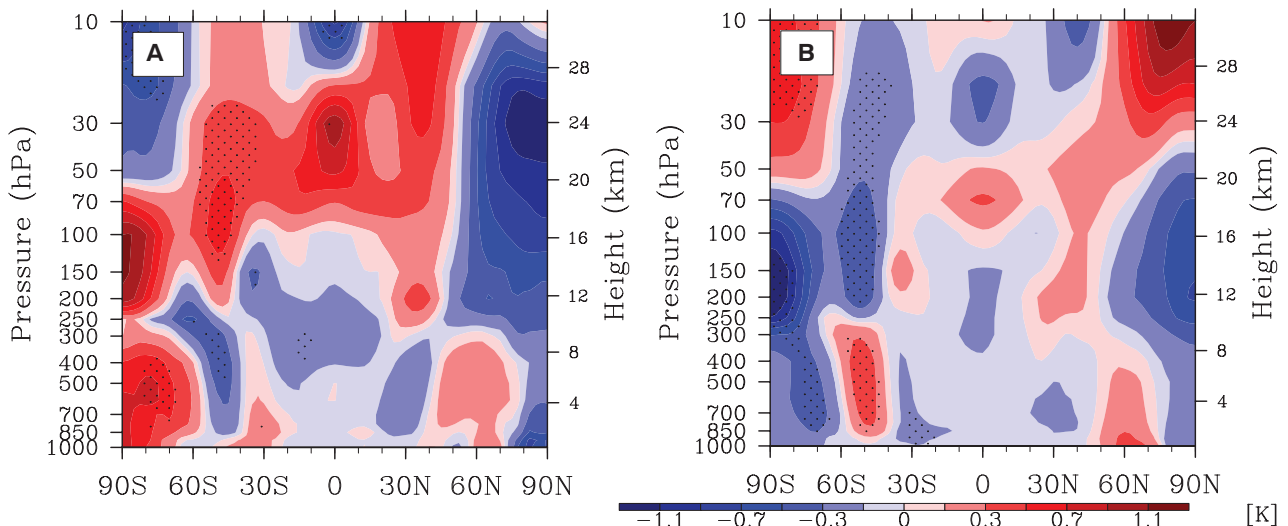


**Fig. 4.** Time-averaged (lag  $-10$  days to  $+10$  days) composite zonal-mean temperature based on (A) SOM1 and (B) SOM3. The dots indicate statistical significance ( $P < 0.05$ ) based on a Student's  $t$  test. For SOM1, the days are chosen only

from ENSO neutral years. Because of the negative SOM1 frequency trend, multiplication of the SOM1 composites by  $-1$  yields the canonical GHG-induced pattern of widespread stratospheric cooling and tropospheric warming.

The SOM1 composite, which is confined to ENSO neutral years (supplementary text; to isolate the influence of non-ENSO processes), shows that in the tropics and mid-latitudes there is widespread warming in the stratosphere and cooling in the troposphere. Because the decadal SOM1 frequency trend is negative, this spatial structure indicates that the long-term temperature trend associated with SOM1 is stratospheric cooling and tropospheric warming. This is indeed consistent with the canonical temperature response to an increased atmospheric loading of GHG. The GHG-induced polar stratospheric temperature changes also match with the findings of modeling studies (26) (supplementary text). For SOM3, there is cooling in the Antarctic lower stratosphere, which is consistent with ozone depletion. All of the above evidence collectively suggests that SOM1 is driven by GHG, whereas SOM3 is driven by ozone.

Although a number of different theories for the jet shift have been proposed (27–30), the mechanism is still a subject of debate because it is difficult to tease apart the proposed causalities. The finding here that the trends are realized through fundamentally short time processes provides an avenue to test the theories in the future. One mechanism that has received limited attention is the impact of tropical convection on the poleward jet shift. Such a mechanism is appealing because it would link two robust trends seen in climate models: (i) intensification of tropical precipitation minus evaporation (hence tropical convection) and (ii) a positive SAM trend (poleward jet shift). Indeed, the SOM1 zonal wind anomalies are established about 10 days after the El Niño-like convection strengthens (figs. S4B and S6), and we found evidence that this connection involves convectively excited Rossby waves. The remaining three SOM patterns are also asso-

ciated with significant ( $P < 0.05$ ) tropical convection anomalies reminiscent of the eastward-propagating convective complex in the tropics known as the Madden-Julian Oscillation. However, a more detailed description of the role of the convection will be reported elsewhere, as doing so is beyond the scope of this report.

The zonal wind evolution (fig. S6) indicates that from lag -5 to lag +5 days SOM1 is accompanied by significant zonal wind anomalies with features close to being symmetric about the equator, particularly within the tropics and subtropics. This quasi-hemispheric symmetry further suggests that tropical convection plays an important role for enabling GHG forcing to influence the mid-latitude jets. For SOM3, extratropical anomalies are first established by lag -15 days. The signal extends into the tropical troposphere by the lag-0 day, and 5 days later it reaches the Arctic troposphere and stratosphere. This picture of a tropical conduit helps to explain the fact that the model responses to Antarctic ozone depletion also produce a substantial response in the Northern Hemisphere (19).

This study shows evidence that the atmospheric response to GHG and stratospheric ozone changes can be distinguished by applying cluster analysis to daily data. We found that the ozone forcing had a greater effect on the jet shift, supporting the modeling results (9, 10). Moreover, this method allows us to estimate the trends caused by each of the forcings. Given the debate over the uncertainty in the ozone recovery (31), we make estimates of the year 2040 1000-hPa zonal-mean zonal wind for the following two limiting scenarios: the first based on the assumption that the ozone concentration will remain at its current value (scenario 1) and the second based on the assumption that the ozone will recover by 2040 (32) (scenario 2). In both scenarios,

we assume that the GHG-driven zonal wind trend will remain at its 1979 to 2008 value. As Table 2 shows, the greatest fractional changes occur between 60° and 67.5°S. At 65°S, close to the coastline of Antarctica where the wind stress change can have a great impact on coastal upwelling, the wind speed would increase by 126% under scenario 1, whereas under scenario 2, the wind speed would decrease to almost zero.

References and Notes

1. J. W. Kidson, *J. Clim.* **12**, 2808 (1999).
2. D. W. J. Thompson, J. M. Wallace, G. C. Hegerl, *J. Clim.* **13**, 1018 (2000).
3. G. J. Marshall, *J. Clim.* **16**, 4134 (2003).
4. J. R. Toggweiler, J. L. Russell, S. R. Carson, *Paleoceanography* **21**, PA2005 (2006).
5. R. F. Anderson *et al.*, *Science* **323**, 1443 (2009).
6. M. Tedesco, A. J. Monaghan, *Geophys. Res. Lett.* **36**, L18502 (2009).
7. V. Limpasuvan, D. L. Hartmann, *Geophys. Res. Lett.* **26**, 3133 (1999).
8. P. J. Kushner, I. M. Held, T. L. Delworth, *J. Clim.* **14**, 2238 (2001).
9. J. M. Arblaster, G. A. Meehl, *J. Clim.* **19**, 2896 (2006).
10. L. M. Polvani, D. W. Waugh, G. J. P. Correa, S.-W. Son, *J. Clim.* **24**, 795 (2011).
11. C. Franzke, S. B. Feldstein, *J. Atmos. Sci.* **62**, 3250 (2005).
12. N. C. Johnson, S. B. Feldstein, B. Tremblay, *J. Clim.* **21**, 6354 (2008).
13. T. Kohonen, *Self-Organizing Maps: Information Science* (Springer, Berlin, 2001).
14. B. C. Dee *et al.*, *Q. J. R. Meteorol. Soc.* **137**, 553 (2011).
15. Materials and methods are available as supplementary materials on Science Online.
16. M. E. Higgins, J. J. Cassano, *J. Geophys. Res.* **114**, D16107 (2009).
17. D. J. Lorenz, E. T. DeWeaver, *J. Geophys. Res.* **112**, D10119 (2007).
18. A. Y. Karpechko, N. P. Gillett, L. J. Gray, M. Dall'Amico, *J. Geophys. Res.* **115**, D22117 (2010).
19. S. M. Kang, L. M. Polvani, J. C. Fyfe, M. Sigmond, *Science* **332**, 951 (2011); 10.1126/science.1202131.
20. A. C. Clement, R. Seager, M. A. Cane, S. E. Zebiak, *J. Clim.* **9**, 2190 (1996).
21. M. A. Cane *et al.*, *Science* **275**, 957 (1997).
22. S. Lee, T. Gong, N. Johnson, S. B. Feldstein, D. Pollard, *J. Clim.* **24**, 4350 (2011).
23. M. L. H'Heureux, D. W. J. Thompson, *J. Clim.* **19**, 276 (2006).
24. T. Gong, S. B. Feldstein, D. Luo, *J. Atmos. Sci.* **67**, 2854 (2010).
25. R. X. Black, B. A. McDaniel, *J. Atmos. Sci.* **64**, 2968 (2007).
26. B. Grassi, G. Redaelli, G. Visconti, *Geophys. Res. Lett.* **33**, L23704 (2005).
27. W. A. Robinson, *J. Clim.* **10**, 176 (1997).
28. L. M. Polvani, P. J. Kushner, *Geophys. Res. Lett.* **29**, 1114 (2002).
29. S.-W. Son, S. Lee, *J. Atmos. Sci.* **62**, 3741 (2005).
30. G. Chen, I. M. Held, *Geophys. Res. Lett.* **34**, L21805 (2007).
31. E. C. Weatherhead, S. B. Andersen, *Nature* **441**, 39 (2006).
32. A. Tabazadeh, E. Cordero, *Atmos. Environ.* **38**, 647 (2004).

**Acknowledgments:** This research was supported by NSF grants AGS-1036858 and AGS-1139970. The authors acknowledge N. Johnson for providing the Matlab codes used for the SOM analysis and two anonymous reviewers for their helpful suggestions and comments.

Supplementary Materials

www.sciencemag.org/cgi/content/full/339/6119/563/DC1  
 Materials and Methods  
 Figs. S1 to S6  
 References (33, 34)  
 24 May 2012; accepted 27 November 2012  
 10.1126/science.1225154

**Table 2.** Projected 1000-hPa zonal-mean zonal wind changes (relative to 1979 to 2008 climatological values) in the year 2040, based on two scenarios: the Antarctic ozone concentration remaining at the current level (scenario 1); the ozone concentration recovering to the pre-1980 value (scenario 2). In both scenarios, it is assumed that the rate of zonal wind change caused by the GHG increase remains at its 1979 to 2008 value.

Latitude (°S)	Scenario 1 (m/s)	Scenario 2 (m/s)	Climatology (m/s)
30.0	-0.13	-0.04	-2.39
32.5	-0.17	0.01	-1.29
35.0	-0.21	0.07	0.13
37.5	-0.22	0.12	2.02
40.0	-0.20	0.15	3.85
42.5	-0.14	0.15	5.42
45.0	-0.06	0.14	6.68
47.5	0.05	0.11	7.40
50.0	0.17	0.06	7.64
52.5	0.27	-0.01	7.42
55.0	0.37	-0.08	6.73
57.5	0.44	-0.15	5.65
60.0	0.47	-0.23	4.07
62.5	0.44	-0.27	2.20
65.0	0.33	-0.23	0.26
67.5	0.18	-0.15	-1.55
70.0	0.08	-0.09	-2.31